Nanoscale

# Electrostatic Assembly of a Multicomponent Peptide/Amphiphile Nanotube



| | |
|---|---|
| Journal: | *Nanoscale* |
| Manuscript ID | NR-ART-07-2023-003482.R1 |
| Article Type: | Paper |
| Date Submitted by the Author: | 03-Oct-2023 |
| Complete List of Authors: | Linville, Jenae; The Ohio State University, Dept. of Chemistry and Biochemistry<br>Mason, McKensie; The Ohio State University,<br>Lopez-Torres, Edgar; The Ohio State University, Dept. of Chemistry and Biochemistry<br>Parquette, Jon; The Ohio State University, Chemistry and Biochemistry |
| | |

# Electrostatic Assembly of a Multicomponent Peptide/Amphiphile Nanotube.

Received 00th January 20xx,
Accepted 00th January 20xx

DOI: 10.1039/x0xx00000x

*Jenae J. Linville,[a] McKensie L. Mason,[a] Edgar U. Lopez-Torres and Jon R. Parquette[a]**

The ability to integrate the elements of a multicomponent nanostructure with nanoscale precision by co-assembly provides a versatile strategy to create novel materials with tunable properties. The search for function in these materials will require new strategies to be developed that control the assembly process, especially for structurally dissimilar components, which often have a propensity to self-sort into non-integrated nanostructures. In this work, two components, a peptide (**1**) and an amphiphile (**2**), were integratively coassembled into a multicomponent nanotube. The interaction between the two components at the supramolecular level was driven by the electrostatic complementarity of the components, which was controlled by the pH-dependent charge of **1**. Characterization of the coassembled nanotube, **1-2**$_{NT}$, was achieved using a combination of TEM, AFM, CLSM and SIM techniques, which showed that both components were colocalized within the nanotube. These studies, in conjunction with CD, IR and fluorescence studies, suggested that **1** and **2** were arranged in partially reorganized, self-sorted domains, which were integrated as laminated nanoribbons that coiled together into the final co-assembled nanotube.

## 1 Introduction

Biological function emerges in Nature from complex structures comprised of components that cooperatively interact, such as within the cell wall, to mediate the processes of life.[1] In particular, self-assembled systems that organize multiple components into orthogonally sorted arrays often exhibit dynamic properties and functions, as exemplified by the mechanical properties of the cellular skeleton.[2] Thus, there has been increasing interest in developing strategies to assemble nanoscale systems comprised of multiple components with hierarchical organization.[3] Multicomponent self-assembly also promises to play an important role in materials science by producing materials with complex, functional applications from simple building blocks.[4] Such co-assembled materials have potential for enhanced properties because the final structure integrates the components with molecular level precision, as compared with systems obtained by the simple mixing of components.[5-8] Effective strategies to control the co-assembly of two or more components into well-defined, hybrid architectures will be required to advance the search for novel function in these nanomaterials.

Multicomponent assembly is challenging to control because many internal factors, such as monomer complementarity and interaction strength, and external conditions determine the outcome of the assembly process.[9] The nature of the interactions between the components at both the monomer and supramolecular levels determine whether the assembly process "narcissistically" sorts the monomers into homogeneous domains,[10-15] or co-assembles them into structures with the components intimately integrated.[16-20] For example, heteroseeds of one component have been used to induce the co-assembly of a second or third monomer into hierarchical[21,22] or blocky sequences[8-33] within a single assembly. This strategy generally requires structurally matched seeds and monomers to allow the seeds to nucleate co-assembly and is less reliable for components with vastly different structures. Thus, it is challenging to induce structurally dissimilar monomers to assemble into multicomponent nanostructures in which the components interact at the supramolecular level. An example of the co-assembly of two, structurally distinct molecules into a laminated network of two self-sorted nanofibers was achieved by seeding a peptide-based hydrogelator on a preformed, lipid nanofiber template. A key factor to create the laminated nanofibers, in preference to a self-sorted, noninteracting network, was to control the rate of peptide seed formation along the template, which was achieved using dynamic oxime exchange.[23]

Electrostatic pairing often guides the spatial organization of peptides co-assembled into multicomponent β-sheet structures.[24] For example, the co-assembly of fibrillar structures, composed of alternating sequences of peptide monomers, has been achieved using oppositely charged peptides, which resist self-assembly alone due to repulsive interactions, but efficiently assemble when combined.[25-29] Electrostatic interactions between different peptide assemblies has proven effective as a strategy to create hierarchical multipeptide assemblies.[30-34] Similarly, multicomponent gels with interacting fiber networks have been created by controlling the gel formation kinetics of monomers with complementary charges.[35,36] We have previously created hierarchical, multilayer nanotube composites using electrostatic interactions between the self-assembled nanotubes with either covalent polymers or single-walled carbon nanotubes.[37-40] More recently, this strategy was extended to the co-assembly of two peptides into a multicomponent network of nanofiber-wrapped nanotubes.[41] Herein, we describe the integrative co-assembly of a multicomponent nanotube comprised of a peptide and an amphiphile that interact electrostatically at the supramolecular scale.

*Department of Chemistry and Biochemistry*
*The Ohio State University*
*100 W. 18th Ave. Columbus, Ohio 43210*
*E-mail: parquette.1@osu.edu*
*Electronic Supplementary Information (ESI) available*

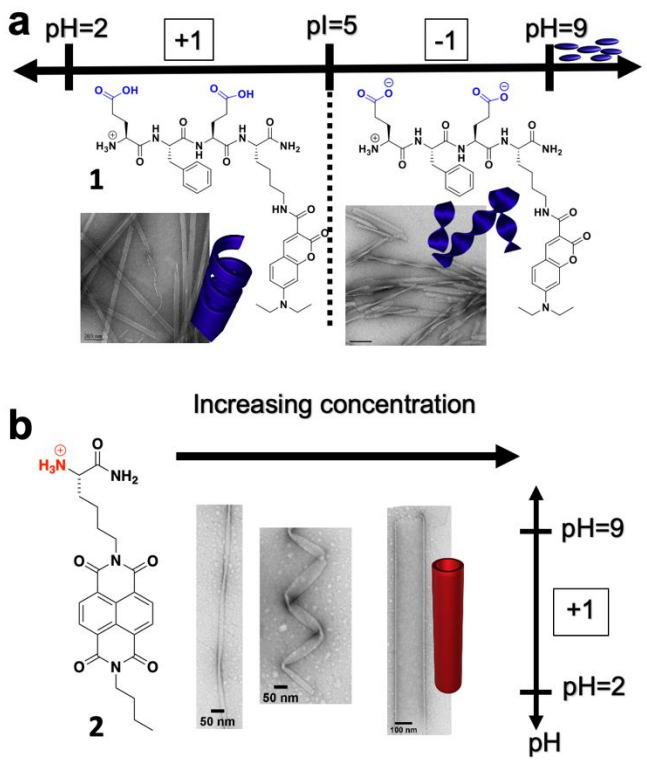


**Fig. 1.** Monocomponent self-assembly of **1** and **2** into nanotubes and nanoribbons. (a) pH-Dependent assembly of **1** into positively charged nanotubes below the pI, negatively charged nanoribbons above the pI and dissociation into a monomeric state at pH >9. (b) Concentration dependent assembly of **2** into nanoribbons and nanotubes ($\mathbf{2}_{NT/NR}$); which was insensitive over pH range of 2-9. TEM image conditions, all aged for 24 h, from left to right: (a) 1 mM of **1** at pH 3.5 and 1 mM of **1** pH 6.5; (b) 1 mM of **2**, 10 mM of **2**, 20 mM of **2**. At lower concentrations, **2** exists as a mixture of nanotube and nanoribbons ($\mathbf{2}_{NT/NR}$)

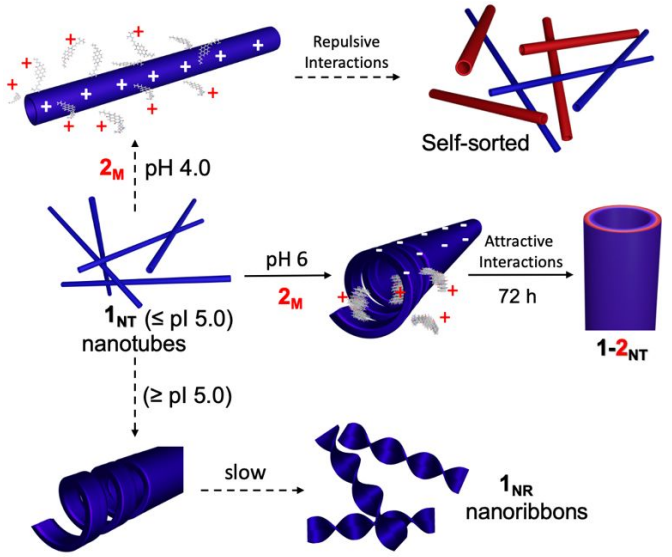


**Fig. 2.** The assembly and co-assembly of **1** and **2**. The transition of nanotubes ($\mathbf{1}_{NT}$) into nanoribbons ($\mathbf{1}_{NR}$) after adjusting to pH 6 (bottom); the assembly of monomeric $\mathbf{2}_M$ in the presence of preformed $\mathbf{1}_{NT}$ at pH 4.0, producing a **self-sorted** mixture of $\mathbf{1}_{NT}$ and $\mathbf{2}_{NT}$ (top) and after adjusting to pH 6.0, leading to **co-assembled** nanotube $\mathbf{1}\text{-}\mathbf{2}_{NT}$ (middle).

## 2 Results and Discussion.

### 2.1 Unimolecular self-assembly of the components.

We investigated the co-assembly of a peptide appended with 4-diethylaminocoumarin (DAC) (EFEK(DAC)-$NH_2$, **1**), with an amphiphilic naphthalenediimide (NDI)-lysine conjugate (Lys(NDI)-$NH_2$, **2**) (Fig. 1). The single-component self-assembly pathways of **1** and **2** were driven by either β-sheet or amphiphilic intermolecular interactions, respectively. These characteristics, along with their distinct structures, imparted a strong predisposition for the monomers to experience self-sorting, rather than co-assembly, upon mixing at the molecular level. However, the pH-dependent charge profile of **1** offered the potential to stimulate charge complementarity at the supramolecular level by pH adjustment. Based on our previous work, peptide **1** exhibited a pH-dependent self-assembly process that produced positively charged, rigid nanotubes ($\mathbf{1}_{NT}$), at pH values below the isoelectric pH (pI 5) and negatively charged, helical nanoribbons ($\mathbf{1}_{NR}$) in the pH range of 6-8.[42] At pH values ≥ 9, the peptide existed in a monomeric state due to intermolecular electrostatic repulsions that attenuated self-assembly. The nanotubes exhibited diameters of 41± 5 nm by TEM, and AFM cross-sectional heights of 10.1 ± 2 nm, reflecting twice the wall dimensions (5 nm). The nanotube walls were composed of two stacked β-sheet aggregates of **1**, which positioned the hydrophobic coumarin and phenylalanine side-chains toward the interior. The amphiphilic self-assembly of **2** produced nanotubes ($\mathbf{2}_{NT}$) via the formation of nanoribbons ($\mathbf{2}_{NR}$) that progressively coiled into nanotubes as the concentration was increased.[43] At low concentrations (<5 mM), **2** assembled into nanoribbons that evolved to a helical tape with a diameter of ~20 nm. At ≥15 mM, the helical tape coiled into nanotubes displaying diameters ranging from 150-300 nm (Fig. 1). In contrast to **1**, the self-assembly of **2** was insensitive to pH values of 2-9.

### 2.2 Co-assembly of 1 and 2: Electrostatic complementarity at the supramolecular level.

To explore the potential of **1** and **2** to electrostatically interact at the supramolecular level, zeta (ζ) potentials were independently measured as a function of pH after self-assembling in water (1 mM) for 24 h. Inspection of the pH-dependent ζ-potential profiles showed that whereas both nanostructures maintained positive potentials at pH 4.0, opposite surface charges of -18 mV (for $\mathbf{1}_{NT}$) and +53 mV (for $\mathbf{2}_{NT/NR}$) were recorded at pH 6.5 (Fig. S1). Accordingly, we explored co-assembly in water as a function of pH values above and below the isoelectric pH of **1** (pI 5.0): pH 3-5, and pH 5-8, where the molecules have the same or opposite charges, respectively (Fig. 2). We reasoned that electrostatic repulsion at pH values below the pI of **1** would lead to isolated, self-sorted nanostructures; whereas values above the pI would induce electrostatic integration at the supramolecular level. Accordingly, equimolar ratios **1** and **2** were introduced into the coassembly mixture in their monomeric and/or assembled starting states in water (1 mM each), then incubated for 24 h at

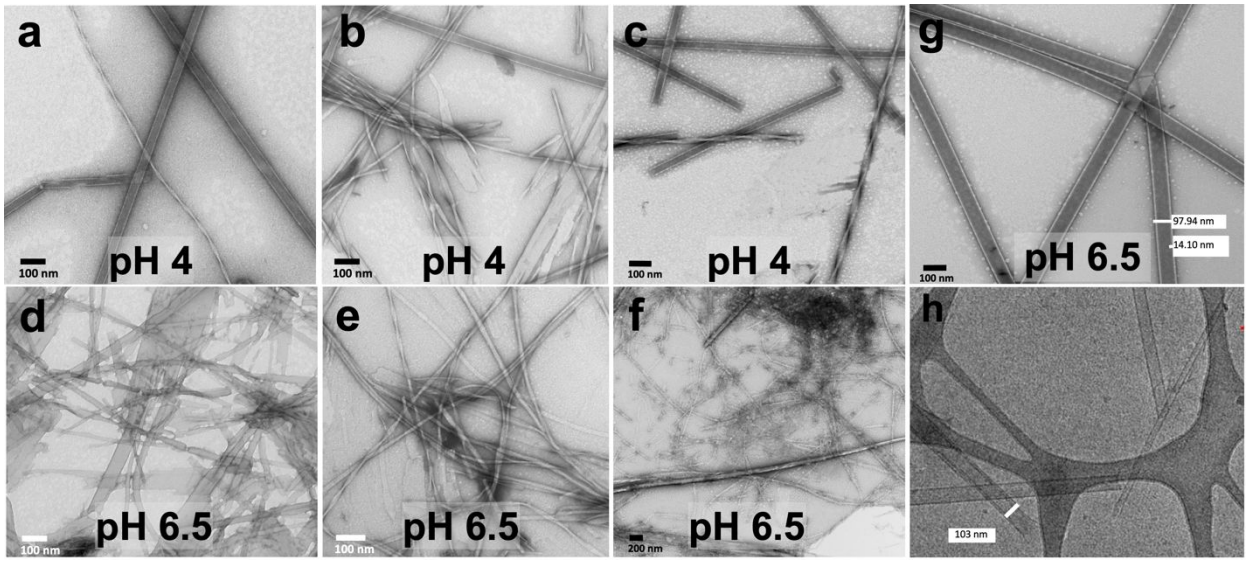


**Fig. 3.** The representative TEM images of **1** and **2** combined at a 1:1 ratio, respectively, at 2 mM (1 mM each), aged for 24 h at either pH 4.0 (a-c) or pH 6.5 (d-g). The components were combined in water and immediately adjusted to pH 4.0 (a-c) or pH 6.5 (d-g) in the following combinations: (a) $\mathbf{1}_M$ + $\mathbf{2}_M$; (b) $\mathbf{1}_{NR}$ +$\mathbf{2}_M$ (c) $\mathbf{1}_{NT}$ + $\mathbf{2}_{NT/NR}$; (d) $\mathbf{1}_M$ + $\mathbf{2}_M$; (e) $\mathbf{1}_{NR}$ + $\mathbf{2}_M$; (f) $\mathbf{1}_{NR}$ + $\mathbf{2}_{NT/NR}$; (g) $\mathbf{1}_{NT}$ + $\mathbf{2}_M$; and (h) Cryo-TEM image of sample prepared by combining $\mathbf{1}_{NT}$ and $\mathbf{2}_M$ (1:1, 2 mM (total), pH 6.5, 3d). The sample was then pelleted by centrifugation (5000 rpm) and redissolved in water (pH 6.5, ~8 mM). Component **1** was converted to monomer by adjusting to pH 9;[42] whereas, **2** was dissociated into a monomeric state by dissolution in TFE and evaporation to a solid powder.[43] Key: $\mathbf{1}_M$ monomer, $\mathbf{1}_{NR}$ nanoribbons, $\mathbf{1}_{NT}$ nanotubes, $\mathbf{2}_M$ monomer, $\mathbf{2}_{NT/NR}$ nanotubes/nanoribbons mixture.

pH 4.0 (Figs. 3a-c). All combinations of **1** and **2** produced mixtures comprised of self-sorted nanostructures formed by the homoassembly of the monomers due to the repulsive electrostatic interactions between the positively charged components at pH 4. Thus, to induce electrostatic attraction between the components, **1** and **2** were combined under pH conditions that exceeded the pI of **1** (pH 6.5) to ensure that the two components were oppositely charged (Figs. 3d-h).[44] Interestingly, all starting conditions at pH 6.5 produced structures that significantly diverged from the self-sorted mixtures observed at pH 4. Notably, as shown in Figure 3g, combining preformed nanotubes of $\mathbf{1}_{NT}$ with monomeric $\mathbf{2}_M$ at pH 6.5 resulted in a nanotube ($\mathbf{1}$-$\mathbf{2}_{NT}$) with dimensions distinct from the single-component nanotubes formed by **1** or **2** alone (Figs. 4a-d & S6).

The co-assembly conditions were then varied with respect to concentration, component ratio, and pH (Figs. S2-5). Although overall concentrations below 2.0 mM (1 mM each) did not produce well-defined nanotubes, increasing the total concentration from 2-4 mM, varying the ratio of **1**:**2** from 1:1 to 1:4, or adjusting the pH in the range of 5.5-6.8 produced similar $\mathbf{1}$-$\mathbf{2}_{NT}$ nanotubes. However, pH values below 5.5 or above 7.3 resulted in degradation of the nanotube structures. Thus, optimal conditions to form homogeneous mixtures of the co-assembled nanotubes were achieved by combining pre-assembled nanotubes of $\mathbf{1}_{NT}$, formed at pH 4 as previously described, with monomeric $\mathbf{2}_M$, in a ratio of 1:1, then immediately adjusting the pH to above the pI of **1** within the range of 5.5 to 6.8 and incubating for 3d. To rule out the potential for artefacts and morphological changes caused by drying or staining during TEM sample preparation, a sample prepared using the optimal conditions was imaged by cryo-TEM,

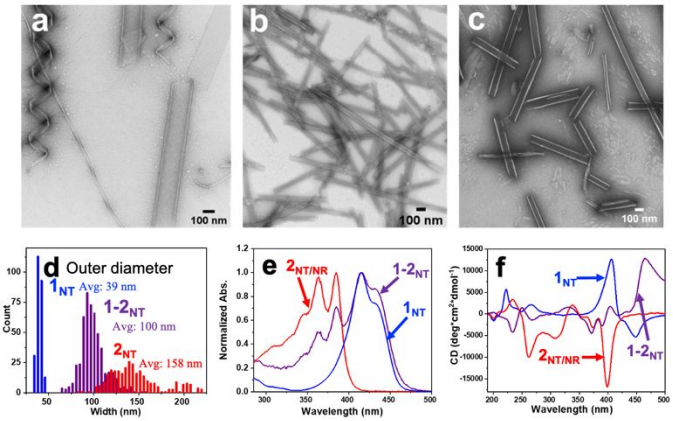


**Fig. 4.** TEM images of (a) **2**, after 1 week at 10 mM at pH 6.5: three assembled states were present: nanofibers, coiled nanoribbons and nanotubes ($\mathbf{2}_{NT/NR}$); (b) **1** aged at pH 3.7 for 24 h at 1 mM exhibiting a homogeneous array of nanotubes ($\mathbf{1}_{NT}$); (c) equimolar mixture of $\mathbf{1}_{NT}$ (1 mM) and $\mathbf{2}_M$ (1 mM) at pH 6.2, then aged for 3d, showing the $\mathbf{1}$-$\mathbf{2}_{NT}$ nanotube; (d) histogram of the diameters of $\mathbf{1}_{NT}$, $\mathbf{2}_{NT}$ and $\mathbf{1}$-$\mathbf{2}_{NT}$ from TEM measurements, averaged over 300-500 nanotubes; (e) UV and (f) CD spectra comparing $\mathbf{2}_{NT/NR}$ (1 mM), $\mathbf{1}_{NT}$ (1mM), and the co-assembled nanotube, $\mathbf{1}$-$\mathbf{2}_{NT}$.

which revealed nanotubes with identical dimensions to those observed by TEM (Figs. 3h & S11). This observation was consistent with the preformed nanotubes ($\mathbf{1}_{NT}$) serving to template the assembly of the monomers of **2**.

To provide insight about the co-assembly process, the co-assembly of **1** and **2** was monitored over time. As shown in Figure 5, ζ-potential measurements taken over 3d revealed a progressive trend toward a value close to zero as **1** and **2** assembled into the $\mathbf{1}$-$\mathbf{2}_{NT}$ nanotube at pH 6.5, as expected for an

electrostatically driven process. The initially negative potential emerged from the positively charged nanotubes of $\mathbf{1}_{NT}$

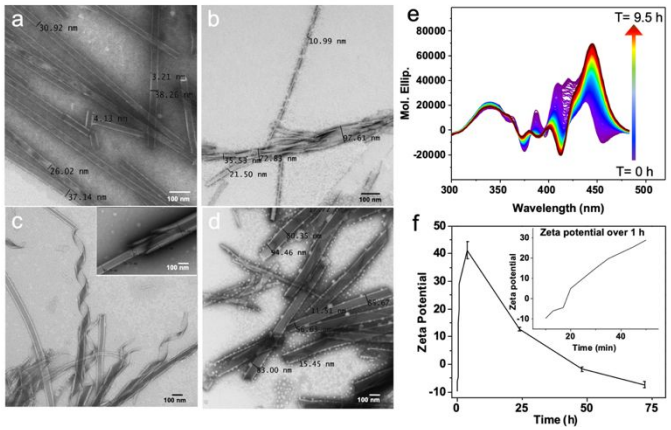


**Fig. 5.** Time-dependent TEM imaging of the co-assembly of $\mathbf{1}_{NT}$ and $\mathbf{2}_{M}$ (2 mM, 1:1, pH 6.4) (a) 30 min., (b) 2.5 h, (c) 24 h and (d) 72 h; (e) CD spectra of co-assembly process over 9.5 h; and (f) z potential measured over 72 h. Inset: z potential progression over 1 h.

(preassembled at pH 4), which became negative as the pH was immediately adjusted to 6.5 after combining the components. The ζ-potential then became positive over an hour as $\mathbf{2}_{M}$, which was introduced in the monomeric state, assembled into positively charged aggregates. The CD spectra and surface potential progressively evolved toward the final state over 3d at pH 6.5 (Figs. 5e-f & S23); whereas, the spectra were invariant over time at pH 4 (Fig. S24). Time-dependent TEM imaging showed that adjusting the pH from 4 to 6.5, after mixing the components, induced the nanotubes of $\mathbf{1}_{NT}$ to partially unwind into sheets, which then recoiled into helical nanoribbons. After ~2.5h, the walls of the ribbons began to thicken and transition over time into the co-assembled nanotubes. These observations along with a progressive increase in AFM cross-sectional heights over 3d (Fig. S22) suggested that the wall thickening reflected the assembly of the monomers of $\mathbf{2}_{M}$ along the coiled nanoribbons of **1**, driven by the electrostatic complementarity of the two components. The addition of increasing amounts of NaCl (2-100 mM) to the co-assembly mixture caused progressive degradation of $\mathbf{1\text{-}2}_{NT}$ and the formation of isolated $\mathbf{1}_{NT}$ nanotubes, consistent with decreasing electrostatic interactions due to charge screening (Figs. S7-8). However, the nanomolar concentrations of NaCl generated during pH adjustments were not sufficient to divert the co-assembly process.

### 2.3 Composition of the co-assembled nanotube, 1-2NT.

The UV-Vis and circular dichroic (CD) spectra were recorded for the co-assembled nanotubes and compared to the spectra of the individually sorted nanostructures of **1** and **2** to provide insight about the composition of $\mathbf{1\text{-}2}_{NT}$ (Figs. 4e-f). The self-assembly of **1** into nanotubes was characterized by the emergence of a split absorbance peak in the range of 400-450 nm with maxima at 415 and 433 nm, corresponding to an excitonic couplet derived from the intermolecular π-stacking of the DAC chromophore. The nanoribbons/nanotubes of **2** featured red-shifted NDI absorptions in the range of 300-400

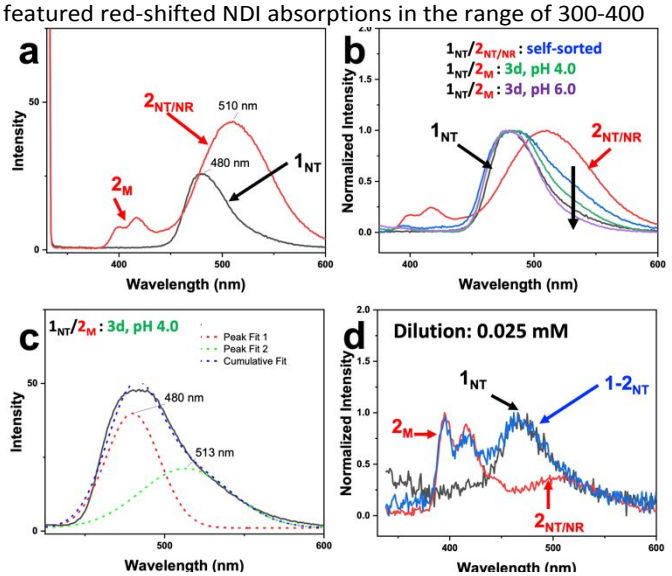


**Fig. 6.** Emission spectra acquired in a triangular quartz cuvette with 330 nm excitation. (a) Emission of $\mathbf{1}_{NT}$ and $\mathbf{2}_{NT/NR}$; (b) emission of $\mathbf{1}_{NT}$ and $\mathbf{2}_{NT/NR}$ compared with a self-sorted, mixture of preassembled $\mathbf{1}_{NT}$ and $\mathbf{2}_{NT/NR}$, a mixture of $\mathbf{1}_{NT}$ and $\mathbf{2}_{M}$, co-assembled for 3d at pH 4.0, and that same mixture adjusted to pH 6.0 prior to aging for 3d; (c) deconvoluted emission of a co-assembled mixture (pH 4.0, 3d) of $\mathbf{1}_{NT}$ and $\mathbf{2}_{M}$ showing two peaks with maximum intensities at 480 nm and 513 nm; and (d) normalized emission of dilutions of **1**, **2** and $\mathbf{1\text{-}2}_{NT}$ at 0.025 mM.

nm, with maxima at 363 nm and 384 nm. Although the co-assembled nanotube displayed UV-Vis absorptions reflecting a superposition of the spectra of both components, the CD spectrum of the nanotube departed significantly from a simple sum of the spectra of self-assembled $\mathbf{1}_{NT}$ and $\mathbf{2}_{NT}$ (Figs. 4e-f, S9). For example, $\mathbf{1}_{NT}$, in nanotube form, exhibited a negative excitonic couplet, reflecting a *P*-type helical twist sense of the coumarin packing interactions, with components centered at ~415 nm and self-assembled **2** showed a large negative CD signal at ~400 nm. A mixture of the two, preassembled components ($\mathbf{1}_{NT}$:$\mathbf{2}_{NT/NR}$ (1:1), 1 mmol each) at pH 4.0 exhibited a CD spectrum resembling a superposition of the spectra of both separately assembled components. In contrast, the co-assembled nanotubes ($\mathbf{1\text{-}2}_{NT}$) (1:1, pH 6.5, 3d) produced a completely different spectrum featuring a prominent, positive peak at 465 nm. The deviation in the CD spectra from that of a perfect superposition indicated a significant change in chromophore packing and organization induced by the interaction between the two components.[45] The peak at 465 nm represents the long wavelength component of a positive excitonic couplet reflecting a *P*-type, helical twist-sense of the coumarin chromophores in **1**.[42] In the monocomponent assemblies of **1**, this couplet was correlated with the formation of nanoribbons at pH 6. The positive component of the negative couplet of $\mathbf{1}_{NT}$ at ~415 nm overlaps with the negative peak exhibited by $\mathbf{2}_{NT/NR}$ at this wavelength, which accounts for the lower intensity of the peaks in this region of the spectra of $\mathbf{1\text{-}2}_{NT}$. Therefore, the spectrum of **1-2NT** might be attributed to a partial reorganization of the *M*-type arrangement of the

coumarins in $\mathbf{1}_{NT}$ to an *P*-type relationship in the co-assembled nanotubes. The partial unwinding of the $\mathbf{1}_{NT}$ nanotubes

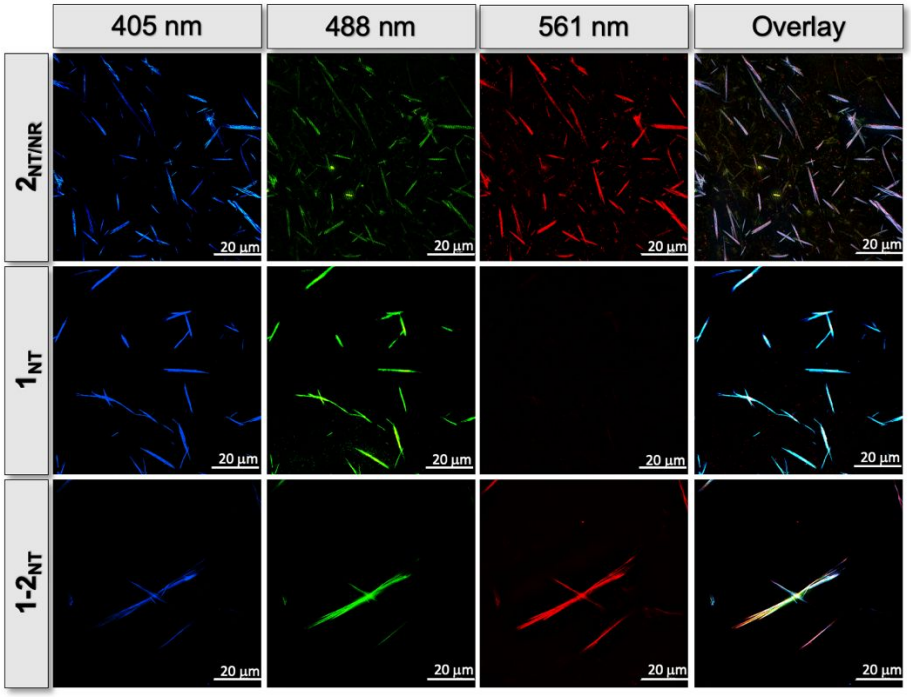


**Fig. 7.** SIM images with 0.2 mol% acridine orange dye added to $\mathbf{2}_{NT/NR}$ (1 mM, top row), $\mathbf{1}_{NT}$ (1 mM, pH 6.5, middle row) and **1-2**$_{NT}$ (2 mM, pH 6.5, bottom), as a function of excitation laser (405 nm-blue, 488 nm-green, and 561 nm-red) and overlayed image of all excitation channels

observed after adjusting the pH to 6.5 was the likely cause for this reorganization in the coumarin packing.

It is noteworthy that the FT-IR spectrum of **1-2**$_{NT}$ indicated that the secondary structure of each component was largely retained in the co-assembled nanotubes, suggesting self-sorting behavior (Fig. S12). For example, the nanotubes (pH 4) and nanoribbons (pH 6.0) of **1** were comprised of primarily β-sheet structure (80%), whereas $\mathbf{2}_{NT}$ existed as random coil (80%). The spectra of the co-assembled nanotubes revealed an approximate 60:40 ratio of β-sheet to random coil structure, suggesting that each component partially retained their structure within the co-assembly. Based on the time evolution of the TEM spectra, along with the CD and IR data, we hypothesize that **1-2**$_{NT}$ nanotubes were formed by the progressive coiling and lateral fusion of self-sorted, laminated ribbons of **1** and **2** that form by electrostatically-driven, templated assembly of $\mathbf{2}_{M}$ along the surface of partially unwound nanotubes of $\mathbf{1}_{NT}$.

### 2.4 Förster resonance energy transfer (FRET).

Analysis of fluorescence spectra of **1** and **2** and the co-assembled mixture of the two provided additional evidence of a close proximity of the components in the co-assembled state. The DAC and NDI fluorescent chromophores in **1** and **2**, respectively, exhibited sufficient spectral overlap for NDI→DAC Förster resonance energy transfer (FRET) to potentially occur (Fig. S13). The J-integral of the overlap of the emission of $\mathbf{2}_{NT/NR}$ and the absorption of $\mathbf{1}_{NT}$ was calculated to be 7.23 x $10^{13}$ ($M^{-1}cm^{-1}nm^4$)(Fig. S15).[46] FRET involves energy transfer through non-radiative, dipole-dipole coupling where the donor fluorophore acts as an oscillator that exchanges energy through space with an acceptor that has a similar resonance frequency.[47] Although the DAC chromophore absorbed only weakly at 330 nm, a small emission band at 480 nm was observed upon excitation at 330 nm; whereas, excitation of $\mathbf{2}_{NT/NR}$ at this wavelength produced small monomer emission bands around 400-430 nm along with a larger excimer peak at 510 nm.[43] The spectra of a self-sorted, physical mixture of pre-assembled forms of $\mathbf{1}_{NT}$ and $\mathbf{2}_{NT/NR}$ exhibited an emission peak at 480 nm along with a broad shoulder, which was deconvoluted into two peaks at ~477 and ~512 nm that overlapped with the emissions of the isolated $\mathbf{1}_{NT}$ and $\mathbf{2}_{NT/NR}$ (Fig. S14). Similarly, performing the co-assembly of $\mathbf{1}_{NT}$ and $\mathbf{2}_{M}$ at pH 4.0, where electrostatic repulsions would preclude a strong interaction between $\mathbf{1}_{NT}$ and $\mathbf{2}_{NT/NR}$, also reduced the amount of energy transfer, producing peaks at ~480 and ~513 nm, after deconvolution (Fig. 6). In contrast, the co-assembled nanotube (**1-2**$_{NT}$) exhibited a peak corresponding to the emission of only DAC, indicative of energy transfer between the NDI and DAC chromophores. Similarly, **1** and **2**, prepared at a low concentration to prevent assembly (0.025 mM), displayed an emission profile that closely matched a simple superposition of the individual spectra. Although significant overlap of the emission spectra of $\mathbf{1}_{NT}$ and $\mathbf{2}_{NT/NR}$ precluded accurate determination of the FRET efficiency, efficiency values, measured at 560 nm to minimize overlap, of samples prepared by co-assembly at pH 6, 4 and self-sorted mixtures were estimated to be ~83, 54 and 58%, respectively (Fig. S15).

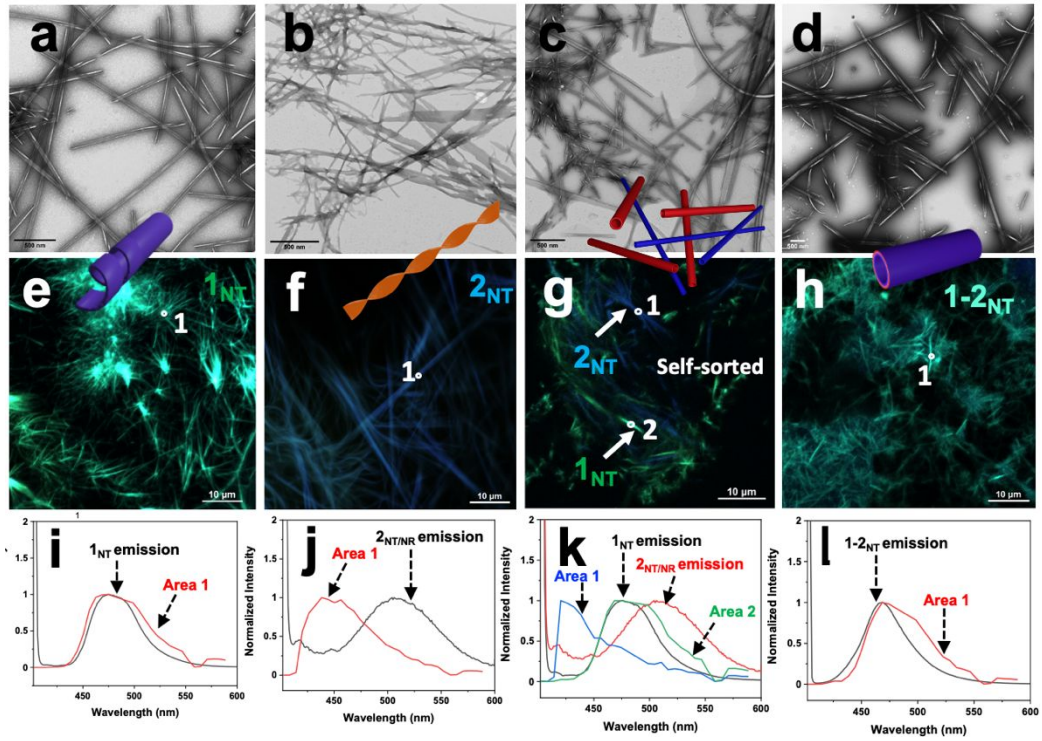


**Figure 8.** TEM images (top row), confocal fluorescence images (middle row), and emission spectra (bottom row) of $\mathbf{1}_{NT}$ (1 mM) (a, e, i); $\mathbf{2}_{NT/NR}$ (1 mM) (b, f, j); a 1:1 mixture of pre-assembled, self-sorted mixture of $\mathbf{1}_{NT}$ (1 mM) (a, e, i) and $\mathbf{2}_{NT/NR}$ (1 mM) (c, g, k), and $\mathbf{1}$-$\mathbf{2}_{NT}$ (d, h, l). Confocal fluorescence images were taken in spectral detector mode, excited at 402 nm, with 6 nm resolution and 32 channels, which were merged together. Emission profiles generated from circled areas of the confocal fluorescence images were compared (bottom row) to emission spectra of same samples acquired using a spectrofluorometer excited at 402 nm, using a triangular quartz cuvette

### 2.5 Structured illumination microscopy (SIM) and confocal laser scanning microscopy (CLSM).

The co-assembled nanotube was further imaged by structured illumination microscopy (SIM) to probe the composition of the structure with nanoscale spatial resolution.[48,49] This imaging technique permits multiple emissive components to be spatially differentiated within an image based on the ability to selectively excite each component with a tunable laser (405, 488, 561, and 647 nm). As shown in Figure S16, emission signals were detected when nanotubes of **1** were excited at 405 and 488 nm, whereas assemblies of **2** were only excited by the 405 nm laser. Images of $\mathbf{1}$-$\mathbf{2}_{NT}$ generated by excitation at either 405 or 488 nm produced images that colocalized when the images were overlayed. This observation confirmed the presence of **1** within the $\mathbf{1}$-$\mathbf{2}_{NT}$ nanotubes and the absence of self-sorted assemblies of **2** within the same image. However, another strategy was necessary to identify **2** within the $\mathbf{1}$-$\mathbf{2}_{NT}$ nanotubes because excitation at 405 nm induced the emission of both **1** and **2** within the image.

Therefore, we explored the addition of excipient fluorescent dyes to selectively bind and illuminate **2** within the sample (Fig. 7). We found that acridine orange (3,6-bis(dimethylamino)acridine, AO),[50] a positively charged dye at pH 6.5 with a hydrophobic-aromatic core, selectively bound to $\mathbf{2}_{NT/NR}$ and did not interact with $\mathbf{1}_{NT}$ at either pH 4 or 6.5. The selective staining of $\mathbf{2}_{NT/NR}$ was noteworthy because, at pH 6.5, the protonated, positive charges of $\mathbf{2}_{NT/NR}$ and AO would be expected to preclude electrostatic binding. However, the predominant interaction of AO with nucleic acids has been shown to be intercalative binding between the base pair stacks; whereas, electrostatic interactions were less important.[51] Thus, the selectivity for **2** likely emerged from the ability of AO to strongly intercalate between the π–π stacks of NDI chromophores, which predominantly stabilized the nanotube structure. As the absorptions of AO were significantly red-shifted relative to **1** and **2**, excitation with the 561 nm laser selectively induced emission of the dye (Fig. S13). Accordingly, solutions of $\mathbf{1}_{NT}$, $\mathbf{2}_{NT/NR}$ (1 mM) and $\mathbf{1}$-$\mathbf{2}_{NT}$ (2 mM) were treated with 0.2 mol % AO and imaged by SIM with excitation at either 405, 488 or 561 nm. Excitation with the 561 nm laser induced emission from $\mathbf{2}_{NT/NR}$ and $\mathbf{1}$-$\mathbf{2}_{NT}$, but not from $\mathbf{1}_{NT}$. Colocalization of the structures illuminated in the 405, 488 and 561 nm channels in the merged images was consistent with the presence of both **1** and **2** within the co-assembled nanotube, $\mathbf{1}$-$\mathbf{2}_{NT}$.

The co-assembled $\mathbf{1}$-$\mathbf{2}_{NT}$ nanotubes were then imaged using confocal microscopy to provide additional evidence for the spatial overlap of **1** and **2** within in the $\mathbf{1}$-$\mathbf{2}_{NT}$ nanotubes (Figs. 8, S17). Although confocal imaging offered lower spatial resolution, the capability to collect specific wavelength regions, upon excitation at 402 nm, permitted the emissions of **1** and **2** to be distinguished within the image. The fluorescence spectra of **1** and **2** overlapped appreciably in the 580-590 nm range, but **1** emitted with much higher intensity than **2** in this region of the

spectrum (Fig. S13). Similarly, **2** displayed an isolated, weak emission in the 400-430 range, and could be selectively imaged in this wavelength range. Collecting the emission ($\lambda_{exc.}$ 402 nm) from 580-590 nm (pseudo color green) produced an image of $\mathbf{1}_{NT}$, but not $\mathbf{2}_{NT/NR}$ (Figs. S17a-b); whereas the region from 400-430 nm (pseudo color blue) only visualized **2** (Figs. S17c-d). Overlaying images of **1-2**$_{NT}$ obtained by collecting the 580-590 nm (green) and 400-430 nm (blue) wavelength ranges in separate channels indicated colocalization of the nanostructures (Figs. S17e-g), thereby confirming the SIM study indicating that **1** and **2** were both present in nanotubes of **1-2**$_{NT}$. The overlay of the emission channels in spectral detector mode produced spectra of localized regions of the images (Figs. 8i-l), which enabled distinction between the DAC emission of $\mathbf{1}_{NT}$ (pseudo color green) and NDI emission of $\mathbf{2}_{NT/NR}$ (pseudo color blue). Whereas both pseudo color blue and green structures were distinguishable in the self-sorted mixture of $\mathbf{1}_{NT}$ and $\mathbf{2}_{NT/NR}$ at pH 4.0; only pseudo color green emission corresponding to $\mathbf{1}_{NT}$ was visible in the co-assembled sample at pH 6.5, in agreement with quenching of the emission of **2** by FRET in Figure 6.

### 2.6 Selective dissociation of 1 from 1-2$_{NT}$.

The pH-responsive assembly of **1** was exploited to selectively remove this component from localized regions of the **1-2**$_{NT}$ nanotubes. Adjusting the pH of the **1-2**$_{NT}$ nanotubes from 6.5 to 9.0 should induce **1** to dissociate from the nanotubes, leaving $\mathbf{2}_{NT}$ intact. The dissociation of **1** from **1-2**$_{NT}$ following the change in pH to 9.0 was monitored in solution by CD and UV-Vis spectroscopy over 2 h, which showed a progressive transition of **1-2**$_{NT}$ to a spectrum characteristic of the $\mathbf{2}_{NT}$ nanotubes (Fig. S18). UV-Vis spectra obtained from the pellet and supernatant of a sample of **1-2**$_{NT}$ that was centrifuged immediately after a pH change to 9.0 showed that most of **1** partitioned into the supernatant in monomeric form, with $\mathbf{2}_{NT}$ residing primarily in the pellet (Fig. S19). This indicated that **1** could indeed be selectively removed using pH, and that the emission of $\mathbf{2}_{NT}$ was restored upon the disassembly of **1,** which decreased the FRET from **2** to **1**. Confocal imaging of a sample of **1-2**$_{NT}$, placed on a microscope slide immediately after the pH was adjusted to 9, revealed nanostructures showing a gradual change in emission color from pseudo color green ($\mathbf{1}_{NT}$) to blue ($\mathbf{2}_{NT}$) over 1.5 h (Fig. S20). Close inspection of an image after 81 min revealed a gradient of green and blue emission along a single structure, reflecting the partial erosion of **1** from one of the **1-2**$_{NT}$ nanotubes (Fig. 9). The slower disassembly of **1** observed by confocal imaging, compared to CD or UV-Vis, likely emerged from the slower diffusion of NaOH on a microscope slide under the imaging conditions. The observation that both components were present on a single nanostructure and that one could be selectively removed suggested that the two components are organized as integrated, self-sorted arrays within the co-assembled nanotube.[52] The pH-induced dissociation of **1** from **1-2**$_{NT}$ was also monitored by TEM imaging over time (Fig. S21). Immediately after the pH change to 9.0, the dimensions of the nanotubes exhibited an average outer diameter of 109.1 nm, an inner diameter of 74.7 nm, and a wall thickness of 10.4 nm. Comparatively, these nanotubes had slightly larger inner and outer diameters but smaller wall thicknesses than **1-2**$_{NT}$, suggesting that the two components of **1-2**$_{NT}$ were integrated as layers within a multi-layer nanotube composite, which changed in dimensions after **1** was removed. Nanotubes emerged over time with progressively larger outer diameters (~300 nm) that more closely resembled the dimensions of single-component nanotubes of $\mathbf{2}_{NT}$.

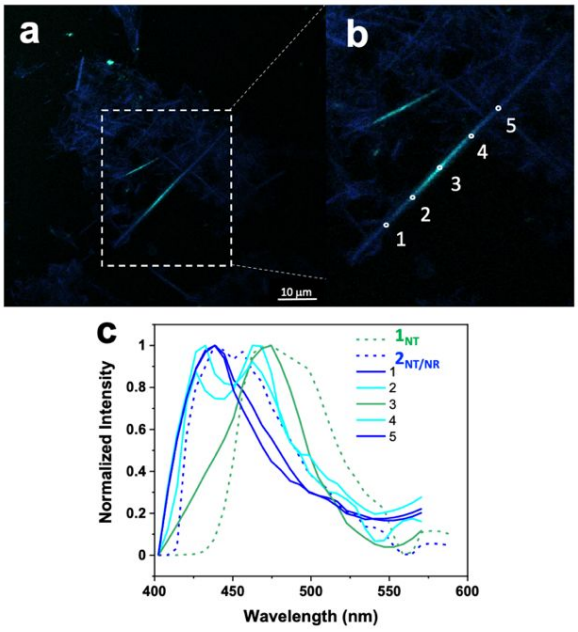


**Fig. 9.** (a) Confocal fluorescence image of a 1:1 co-assembled mixture of $\mathbf{1}_{NT}$ and $\mathbf{2}_{M}$, aged 3 d at pH 6.5 then adjusted to pH 9.0 and immediately placed on a glass slide for 81 minutes and imaged. The image was taken in spectral detector mode, excited at 402 nm, with 6 nm resolution and 32 channels, which were merged together. (c) Emission profiles were generated along the structure and compared to those obtained for $\mathbf{1}_{NT}$ and $\mathbf{2}_{NT/NR}$, indicating that the emission from both compounds was detected on the same nanostructure.

## 3 Conclusions

In summary, we have demonstrated the co-assembly of an integrative, self-sorted nanotube composed of two components: a peptide (**1**) and an amphiphile (**2**). The co-assembly of molecules with distinct structural features that undergo assembly via different mechanisms is hampered by their tendency to self-sort into non-integrated nanostructures. Integrative co-assembly was driven by electrostatic complementarity of the two components, which was controlled by the pH-dependent charge of **1**. The two components were co-assembled as a mixture of nanotubes of **1**, formed by self-assembly at pH 4.0, and monomeric **2**, then adjusted to a pH of 6.0 to induce electrostatic complementarity. Colocalization of both components within the co-assembled nanotube, **1-2**$_{NT}$, was confirmed using a combination of TEM, AFM, CLSM and SIM techniques. These studies suggest that **1** and **2** were organized into self-sorted domains that were integrated as laminated nanoribbons, which coiled together into the final co-assembled nanotube. The CD spectra of **1-2**$_{NT}$ indicated that significant

reorganization of the components occurred in the process, compared with their self-sorted structures, as the spectra were not a simple superposition of the spectra of both self-assembled components.

## Conflicts of interest

There are no conflicts to declare.

## Acknowledgements

This material is based upon work supported by the National Science Foundation (CHE-2106924). Electron microscopy was performed at the Center for Electron Microscopy and Analysis (CEMAS) at The Ohio State University. We also acknowledge resources from the Campus Microscopy and Imaging Facility (CMIF) and the OSU Comprehensive Cancer Center (OSUCCC) Microscopy Shared Resource (MSR), The Ohio State University. This facility is supported in part by grant P30 CA016058, National Cancer Institute, Bethesda, MD

## Notes and references

1. E. Karsenti, Self-organization in cell biology: a brief history *Nat. Rev. Mol. Cell Bio.*, 2008, **9**, 255-262.
2. Q. W. Liu, B. X. Jin, Q. Li, H. Z. Yang, Y. J. Luo and X. Y. Li, Self-sorting assembly of artificial building blocks *Soft Matter*, 2022, **18**, 2484-2499.
3. K. C. Elbert, T. Vo, D. Oh, H. Bharti, S. C. Glotzer and C. B. Murray, Evaporation-Driven Coassembly of Hierarchical, Multicomponent Networks *ACS Nano.*, 2022, **16**, 4508-4516.
4. A. Joshi, N. Singh and G. Verma, in *Fabrication and Self-Assembly of Nanobiomaterials*, ed. A. M. Grumezescu, William Andrew Publishing, 2016, DOI: https://doi.org/10.1016/B978-0-323-41533-0.00002-7, pp. 29-55.
5. M. Eder, S. Amini and P. Fratzl, Biological composites-complex structures for functional diversity *Science*, 2018, **362**, 543-547.
6. C. Li, A. Iscen, H. Sai, K. Sato, N. A. Sather, S. M. Chin, Z. Alvarez, L. C. Palmer, G. C. Schatz and S. I. Stupp, Supramolecular-covalent hybrid polymers for light-activated mechanical actuation *Nat. Mater.*, 2020, **19**, 900-909.
7. C. Colquhoun, E. R. Draper, E. G. B. Eden, B. N. Cattoz, K. L. Morris, L. Chen, T. O. McDonald, A. E. Terry, P. C. Griffiths, L. C. Serpell and D. J. Adams, The effect of self-sorting and co-assembly on the mechanical properties of low molecular weight hydrogels *Nanoscale*, 2014, **6**, 13719-13725.
8. A. K. Patterson and D. K. Smith, Two-component supramolecular hydrogel for controlled drug release *Chem. Commun.*, 2020, **56**, 11046-11049.
9. L. Li, R. Sun and R. Zheng, Tunable morphology and functionality of multicomponent self-assembly: A review *Mater. Des.*, 2021, **197**, 109209.
10. J. Boekhoven, A. M. Brizard, M. C. A. Stuart, L. Florusse, G. Raffy, A. Del Guerzo and J. H. van Esch, Bio-inspired supramolecular materials by orthogonal self-assembly of hydrogelators and phospholipids *Chem. Sci.*, 2016, **7**, 6021-6031.
11. R. Kubota, S. Liu, H. Shigemitsu, K. Nakamura, W. Tanaka, M. Ikeda and I. Hamachi, Imaging-Based Study on Control Factors over Self-Sorting of Supramolecular Nanofibers Formed from Peptide- and Lipid-type Hydrogelators *Bioconjug. Chem.*, 2018, **29**, 2058-2067.
12. C. Felip-León, S. Díaz-Oltra, F. Galindo and J. F. Miravet, Chameleonic, Light Harvesting Photonic Gels Based on Orthogonal Molecular Fibrillization *Chem. Mater.*, 2016, **28**, 7964-7972.
13. K. L. Morris, L. Chen, J. Raeburn, O. R. Sellick, P. Cotanda, A. Paul, P. C. Griffiths, S. M. King, R. K. O'Reilly and L. C. Serpell, Chemically programmed self-sorting of gelator networks *Nat. Commun.*, 2013, **4**, 1480.
14. E. R. Draper, J. R. Lee, M. Wallace, F. Jäckel, A. J. Cowan and D. J. Adams, Self-sorted photoconductive xerogels *Chem. Sci.*, 2016, **7**, 6499-6505.
15. D. J. Cornwell, O. J. Daubney and D. K. Smith, Photopatterned Multidomain Gels: Multi-Component Self-Assembled Hydrogels Based on Partially Self-Sorting 1,3:2,4-Dibenzylidene-D-sorbitol Derivatives *J. Am. Chem. Soc.*, 2015, **137**, 15486-15492.
16. K. V. Rao, K. Jayaramulu, T. K. Maji and S. J. George, Supramolecular hydrogels and high-aspect-ratio nanofibers through charge-transfer-induced alternate coassembly *Angew. Chem. Int. Ed.*, 2010, **49**, 4218-4222.
17. M. A. Khalily, G. Bakan, B. Kucukoz, A. E. Topal, A. Karatay, H. G. Yaglioglu, A. Dana and M. O. Guler, Fabrication of Supramolecular n/p-Nanowires *via* Coassembly of Oppositely Charged Peptide-Chromophore Systems in Aqueous Media *ACS Nano.*, 2017, **11**, 6881-6892.
18. H. Frisch, J. P. Unsleber, D. Ludeker, M. Peterlechner, G. Brunklaus, M. Waller and P. Besenius, pH-Switchable ampholytic supramolecular copolymers *Angew. Chem. Int. Ed.*, 2013, **52**, 10097-10101.
19. M. Tena-Solsona, S. Alonso-de Castro, J. F. Miravet and B. Escuder, Co-assembly of tetrapeptides into complex pH-responsive molecular hydrogel networks *J. Mater. Chem. B*, 2014, **2**, 6192-6197.
20. D. Gorl, X. Zhang, V. Stepanenko and F. Wurthner, Supramolecular block copolymers by kinetically controlled co-self-assembly of planar and core-twisted perylene bisimides *Nat. Commun.*, 2015, **6**, 7009.
21. Y. Liu, C. Peng, W. Xiong, Y. Zhang, Y. Gong, Y. Che and J. Zhao, Two-Dimensional Seeded Self-Assembly of a Complex Hierarchical Perylene-Based Heterostructure *Angew. Chem. Int. Ed.*, 2017, **56**, 11380-11384.
22. Y. Liu, Y. Gong, Y. Guo, W. Xiong, Y. Zhang, J. Zhao, Y. Che and I. Manners, Emergent Self-Assembly Pathways to Multidimensional Hierarchical Assemblies using a Hetero-Seeding Approach *Chem. Eur. J.*, 2019, **25**, 13484-13490.
23. R. Kubota, K. Nagao, W. Tanaka, R. Matsumura, T. Aoyama, K. Urayama and I. Hamachi, Control of seed formation allows two distinct self-sorting patterns of supramolecular nanofibers *Nat. Commun.*, 2020, **11**, 4100.
24. D. T. Seroski, X. Dong, K. M. Wong, R. Liu, Q. Shao, A. K. Paravastu, C. K. Hall and G. A. Hudalla, Charge guides pathway selection in beta-sheet fibrillizing peptide co-assembly *Commun. Chem.*, 2020, **3**, 172.
25. D. M. Raymond and B. L. Nilsson, Multicomponent peptide assemblies *Chem. Soc. Rev.*, 2018, **47**, 3659-3720.
26. M. Tena-Solsona, S. Alonso-de Castro, J. F. Miravet and B. Escuder, Co-assembly of tetrapeptides into complex pH-responsive molecular hydrogel networks *J. Mater. Chem. B*, 2014, **2**, 6192-6197.

27. B. Soto Morales, R. Liu, J. Olguin, A. M. Ziegler, S. M. Herrera, K. L. Backer-Kelley, K. L. Kelley and G. A. Hudalla, Injectable nanofibrillar hydrogels based on charge-complementary peptide co-assemblies *Biomater. Sci.*, 2021, **9**, 2494-2507.
28. K. Roy, M. Chetia, A. K. Sarkar and S. Chatterjee, Co-assembly of charge complementary peptides and their applications as organic dye/heavy metal ion (Pb(2+), Hg(2+)) absorbents and arsenic(iii/v) detectors *RSC Adv*, 2020, **10**, 42062-42075.
29. K. Gayen, N. Nandi, K. S. Das, D. Hermida-Merino, I. W. Hamley and A. Banerjee, The aging effect on the enhancement of thermal stability, mechanical stiffness and fluorescence properties of histidine-appended naphthalenediimide based two-component hydrogels *Soft Matter*, 2020, **16**, 10106-10114.
30. J. R. Wester, J. A. Lewis, R. Freeman, H. Sai, L. C. Palmer, S. E. Henrich and S. I. Stupp, Supramolecular Exchange among Assemblies of Opposite Charge Leads to Hierarchical Structures *J. Am. Chem. Soc.*, 2020, **142**, 12216-12225.
31. D. Wang, X. Hou, X. Zhang, Y. Zhao, B. Ma, Y. Sun and J. Wang, Light- and pH-Controlled Hierarchical Coassembly of Peptide Amphiphiles *Langmuir*, 2019, **35**, 9841-9847.
32. I. W. Hamley, A. Dehsorkhi and V. Castelletto, Coassembly in Binary Mixtures of Peptide Amphiphiles Containing Oppositely Charged Residues *Langmuir*, 2013, **29**, 5050-5059.
33. S. Li, A. K. Mehta, A. N. Sidorov, T. M. Orlando, Z. Jiang, N. R. Anthony and D. G. Lynn, Design of Asymmetric Peptide Bilayer Membranes *J. Am. Chem. Soc.*, 2016, **138**, 3579-3586.
34. I. Cohen-Erez and H. Rapaport, Coassemblies of the Anionic Polypeptide gamma-PGA and Cationic beta-Sheet Peptides for Drug Delivery to Mitochondria *Biomacromolecules*, 2015, **16**, 3827-3835.
35. S. Panja, A. Seddon and D. J. Adams, Controlling hydrogel properties by tuning non-covalent interactions in a charge complementary multicomponent system *Chem. Sci.*, 2021, **12**, 11197-11203.
36. W. Edwards and D. K. Smith, Enantioselective component selection in multicomponent supramolecular gels *J. Am. Chem. Soc.*, 2014, **136**, 1116-1124.
37. M. Ji, M. B. Dawadi, A. R. LaSalla, Y. Sun, D. A. Modarelli and J. R. Parquette, Strategy for the Co-Assembly of Co-Axial Nanotube-Polymer Hybrids *Langmuir*, 2017, **33**, 9129-9136.
38. M. Ji, M. L. Mason, D. A. Modarelli and J. R. Parquette, Threading carbon nanotubes through a self-assembled nanotube *Chem. Sci.*, 2019, **10**, 7868-7877.
39. M. Ji, B. Daniels, A. Shieh, D. A. Modarelli and J. R. Parquette, Controlling the length of self-assembled nanotubes by sonication followed by polymer wrapping *Chem. Commun.*, 2017, **53**, 12806-12809.
40. M. Ji and J. R. Parquette, Enhanced Stability of Peptide Nanofibers Coated with a Conformal Layer of Polydopamine *Chem. Eur. J.*, 2020, **26**, 8572-8578.
41. M. L. Mason, T. Lin, J. J. Linville and J. R. Parquette, Co-assembly of a multicomponent network of nanofiber-wrapped nanotubes *Nanoscale*, 2022, **14**, 4531-4537.
42. M. L. Mason, R. F. Lalisse, T. J. Finnegan, C. M. Hadad, D. A. Modarelli and J. R. Parquette, pH-Controlled Chiral Packing and Self-Assembly of a Coumarin Tetrapeptide *Langmuir*, 2019, **35**, 12460-12468.
43. H. Shao, M. Gao, S. H. Kim, C. P. Jaroniec and J. R. Parquette, Aqueous Self-Assembly of L-Lysine-Based Amphiphiles into 1D n-Type Nanotubes *Chem. Eur. J.*, 2011, **17**, 12882-12885.
44. V. K. Pal, R. Jain and S. Roy, Tuning the Supramolecular Structure and Function of Collagen Mimetic Ionic Complementary Peptides via Electrostatic Interactions *Langmuir*, 2020, **36**, 1003-1013.
45. G. Gottarelli, S. Lena, S. Masiero, S. Pieraccini and G. P. Spada, The use of circular dichroism spectroscopy for studying the chiral molecular self-assembly: an overview *Chirality*, 2008, **20**, 471-485.
46. A. Langlois and P. D. Harvey, Maple™-assisted calculations of the J-integral: a key parameter for the understanding of excited state energy transfer in porphyrins and other chromophores *J. Porphyr. Phthalocya.*, 2014, **18**, 666-674.
47. J. R. Lakowicz, in *Principles of Fluorescence Spectroscopy*, Springer US, 3 edn., 2006, DOI: 10.1007/978-0-387-46312-4, ch. 443-475, p. 954.
48. R. Kubota, W. Tanaka and I. Hamachi, Microscopic Imaging Techniques for Molecular Assemblies: Electron, Atomic Force, and Confocal Microscopies *Chem. Rev.*, 2021, **121**, 14281-14347.
49. R. Kubota, K. Nakamura, S. Torigoe and I. Hamachi, The Power of Confocal Laser Scanning Microscopy in Supramolecular Chemistry: In situ Real-time Imaging of Stimuli-Responsive Multicomponent Supramolecular Hydrogels *ChemistryOpen*, 2020, **9**, 67-79.
50. M. P. Thome, E. C. Filippi-Chiela, E. S. Villodre, C. B. Migliavaca, G. R. Onzi, K. B. Felipe and G. Lenz, Ratiometric analysis of Acridine Orange staining in the study of acidic organelles and autophagy *J. Cell Sci.*, 2016, **129**, 4622-4632.
51. M. Sayed, B. Krishnamurthy and H. Pal, Unraveling multiple binding modes of acridine orange to DNA using a multispectroscopic approach *Phys. Chem. Chem. Phys.*, 2016, **18**, 24642-24653.
52. S. L. Higashi, K. M. Hirosawa, K. G. N. Suzuki, K. Matsuura and M. Ikeda, One-Pot Construction of Multicomponent Supramolecular Materials Comprising Self-Sorted Supramolecular Architectures of DNA and Semi-Artificial Glycopeptides *ACS Appl. Bio Mater.*, 2020, **3**, 9082-9092.